

Automated Force Free Flux Rope Identification

A. W. Smith¹, J. A. Slavin², C. M. Jackman¹, R. C. Fear¹, G.-K. Poh², G. A. DiBraccio³,
J. M. Jasinski², L. Trenchi¹

¹Department of Physics and Astronomy, University of Southampton, Southampton, UK,

²Climate and Space Sciences and Engineering, University of Michigan, Ann Arbor, MI 48109, USA

³Solar System Exploration Division, NASA Goddard Space Flight Center, Greenbelt, Maryland, USA

Key Points:

- Technique developed to locate cylindrical, quasi-force free flux ropes in magnetometer data.
- Method uses wavelet analysis, minimum variance analysis and a constant- α force free flux rope model.
- Technique successfully applied to MESSENGER data from the Hermean magnetotail.

Author Manuscript

This is the author manuscript accepted for publication and has undergone full peer review but has not been through the copyediting, typesetting, pagination and proofreading process, which

Corresponding author: A. W. Smith, AW.Smith@soton.ac.uk
may lead to differences between this version and the Version of Record. Please cite this article as doi: [10.1002/2016JA022994](https://doi.org/10.1002/2016JA022994)

Abstract

We describe a method developed to automatically identify quasi-force free magnetotail flux ropes from *in-situ* spacecraft magnetometer data. The method locates significant (greater than 1σ) deflections of the north-south component of the magnetic field coincident with enhancements in other field components. The magnetic field data around the deflections are then processed using Minimum Variance Analysis (MVA) to narrow the selection down to those that exhibit the characteristics of flux ropes. The subset of candidates that fulfill the requirements are then compared to a cylindrical, linear (constant- α) force free model. Those that can be well approximated as force-free are then accepted. The model fit also provides a measure of the physical parameters that describe the flux rope (i.e. core field and radius). This process allows for the creation of a repeatable, consistent catalog of flux ropes. Automation allows a greater volume of data to be covered, saving time and allowing the exploration of potential selection biases. The technique is applied to MESSENGER magnetometer data in the Hermean magnetotail and successfully locates flux ropes, some of which match previously known encounters. Assumptions of the method and potential future applications are discussed.

1 Introduction

Magnetic reconnection is an ubiquitous process throughout the magnetized plasmas of the solar system. It is a fundamental mechanism by which energy can be transferred from magnetic fields to the surrounding plasma. In the context of a planetary magnetosphere reconnection is most commonly observed at the magnetopause and in the magnetotail current sheet. Reconnection at the magnetopause can cause mass and flux to be added to the magnetospheric system (from the solar wind), while reconnection of the adjacent anti-parallel fields at the magnetotail current sheet can result in the loss of mass and/or magnetic flux from the system.

In two dimensions, the presence of one or more reconnection x-lines on closed field lines leads to the generation of magnetic islands, or loops [Schindler, 1974]. At the center of a magnetic loop the field strength is zero. When considering three dimensional systems, the formation of magnetic loops requires precisely anti-parallel fields. At Earth and Mercury the magnetic fields within the northern and southern lobes of the magnetotail are often found to be sheared: a result of the interaction between the solar wind and the magnetosphere [Cowley, 1981]. The presence of a shear generates a component of the magnetic field in the azimuthal direction across the current sheet; this can act as a guide field during reconnection, potentially resulting in the formation of flux ropes [Hughes and Sibeck, 1987], however this is still an ac-

45 tive area of research [e.g. *Borg et al.* [2012]]. Flux rope-type plasmoids consist of a series of
46 nested helical magnetic fields forming a cylindrical structure [*Lepping et al.*, 1990].

47 On the magnetospheric scale reconnection forms part of a process by which plasma, mag-
48 netic flux and energy can be transported from the dayside magnetopause into the magnetotail
49 known as the Dungey cycle [*Dungey*, 1961]. In this cycle magnetospheric flux is opened at
50 the planet's dayside magnetopause via reconnection with the interplanetary magnetic field (IMF)
51 in the incoming solar wind. The newly generated open field lines, which map from the planet
52 to the solar wind, are swept across the polar regions into the magnetotail lobes. Meanwhile,
53 reconnection in the magnetotail current sheet can close the oppositely directed lobe fields. The
54 cycle is completed as the closed field lines convect around the flanks to return to the dayside
55 of the planet.

56 As the closest planet to the Sun, and possessing a relatively small magnetosphere (com-
57 pared to the other magnetized planets), Mercury is particularly susceptible to variations in the
58 solar wind, changes that can drive the Dungey cycle. Due to the small spatial scales involved,
59 the cycle operates over dramatically shorter timescales, of the order of ~ 2 to 3 minutes [*Sis-
60 coe et al.*, 1975; *Slavin et al.*, 2010; *Sun et al.*, 2015], compared to ~ 1 to 3 hours at Earth
61 [*Alkafifi*, 1964; *Baker et al.*, 1996; *Huang*, 2002]. Similarly, the average duration of magne-
62 totail flux rope observations with the MESSENGER (MErcury Surface, Space ENvironment,
63 GEochemistry, and Ranging) spacecraft at Mercury was found to be 0.74 s [*DiBraccio et al.*,
64 2015], much shorter than the 30 s to 2 minute durations observed at the Earth [*Ieda et al.*, 1998;
65 *Slavin et al.*, 2003a].

66 Historically, surveys of plasmoids and flux ropes in Earth's magnetotail have been per-
67 formed by visual inspection of spacecraft data [e.g. *Scholer et al.* [1984]; *Richardson et al.* [1987];
68 *Moldwin and Hughes* [1992]; *Ieda et al.* [1998]; *Slavin et al.* [2003a]]. Criteria based on the
69 magnetic field and local plasma environment were developed and applied by eye to create self-
70 consistent catalogs. Similarly, several studies of flux ropes in the magnetotail of Mercury have
71 been performed [*Slavin et al.*, 2009, 2012; *DiBraccio et al.*, 2015]. Unlike at the Earth, where
72 high-resolution plasma data is generally available, these studies have relied more heavily on
73 the magnetometer data to identify these structures. Again, selection criteria were applied man-
74 ually, and each event processed individually. This has worked very well in both environments,
75 however it is hugely time consuming and difficult to keep the selection process completely con-
76 sistent; separate authors may well select marginally different subsets of events.

77 Some studies have begun to introduce some degree of automation to the process of plas-
78 moid identification; e.g. for locating periods when the north-south component of the magnetic
79 field is enhanced above background levels [Vogt *et al.*, 2010; Jackman *et al.*, 2014], or to find
80 significant deflections of the field [Smith *et al.*, 2016]. Automated techniques have also been
81 used to identify magnetopause flux transfer events (FTEs) via bipolar field deflections [e.g. Kawano
82 and Russell, 1996], albeit still requiring manual confirmation. Karimabadi *et al.* [2007] intro-
83 duced a data mining technique (MineTool), and later applied it to locate FTEs [Karimabadi
84 *et al.*, 2009], using a combination of magnetic field and plasma data. Recently, Malaspina and
85 Gosling [2012] refined a technique to identify rotational discontinuities in the STEREO so-
86 lar wind data using the gradient of the magnetic field (the method was initially developed by
87 Vasquez *et al.* [2007]). These techniques are well designed to pick out large scale rotations a
88 single field component. Flux rope signatures, however, are complex and require coordinated
89 changes in multiple field components.

90 We present a fully automated technique designed to identify *in-situ* observations of lin-
91 ear (constant α) force-free magnetotail flux ropes in spacecraft magnetometer data. The method
92 includes several widely used analysis methods, which when combined reliably and repeatably
93 identify flux ropes signatures. The automation both reduces the subjectivity of flux rope sur-
94 veys and enables the application of Minimum Variance Analysis (MVA) and force-free model
95 fitting to large ensembles of flux ropes.

96 The technique has been developed using MESSENGER magnetometer data, however it
97 could be applied to other data sets with some adaptation. Below we summarize the dataset used,
98 the expected magnetic field signature in the data and the flux rope model selected. The pro-
99 cess is then discussed with reference to an example detection and several trial intervals. As-
100 sumptions and potential adaptations are then discussed.

101 **2 Data, Signatures and Model**

102 **2.1 Data**

103 The method was developed using magnetometer data from the MESSENGER (MErcury
104 Surface, Space ENvironment, GEochemistry, and Ranging) spacecraft [Solomon *et al.*, 2007;
105 Anderson *et al.*, 2007]. Data with a cadence of 20 Hz were used; the short timescales of flux
106 ropes (~ 0.74 s [DiBraccio *et al.*, 2015]) necessitate the use of high resolution data. MES-
107 SENDER orbited Mercury from 18th March 2011 until 30th April 2015. During this time it

performed highly inclined, eccentric orbits with a period of ~ 12 hours (later reduced to ~ 8 hours). This orbit caused MESSENGER to make approximately vertical cuts through the magnetotail plasma sheet several times a day during certain seasons. It is within ~ 25 of these plasma sheet crossings that the process was tested and developed. These crossings are located in the near-Mercury tail, close to midnight in the tail plasma sheet. Orbits were carefully selected to ensure the detections related to flux ropes and not to other processes that occur closer to the magnetopause.

The magnetometer data were used in the aberrated Mercury-Solar-Magnetospheric (henceforth MSM) coordinate system. In this Cartesian system the z-axis (\hat{Z}_{MSM}) is aligned with the dipole axis pointing north, the x-direction (\hat{X}_{MSM}) traces the Mercury-Sun direction and the y-axis (\hat{Y}_{MSM}) completes the right handed set. At Mercury the dipole and rotational axes are approximately aligned, however the magnetic equatorial plane (described by \hat{X}_{MSM} and \hat{Y}_{MSM}) is offset north from the planet's geometrical center by $\sim 0.2 R_M$ [Anderson et al., 2011]. The magnetic field data were corrected for solar wind aberration (aberrated coordinates are indicated with '' notation). This was accomplished using the local orbital velocity of Mercury and assuming a solar wind velocity of 425 km s^{-1} .

2.2 Magnetotail Flux Rope Signatures

Previous studies have found that flux ropes largely lie in the \hat{X} - \hat{Y} plane [Slavin et al., 2003a], generally with their axis in the $\pm \hat{Y}$ direction, traveling in the $\pm \hat{X}$ direction (planetward or tailward) due to the prevailing tail configuration [DiBraccio et al., 2015]. If a flux rope were to pass directly over the spacecraft with this approximate orientation and velocity then a magnetometer would observe: a bipolar variation in B_Z , a local maximum in B_Y (corresponding to the strong core field along the axis) and a peak in the total field magnitude ($|B|$).

If the spacecraft passes directly through the center of a flux rope then the deflection in B_Z^{MSM} will be symmetrical and bipolar. However, if the spacecraft's passage through the flux rope is offset then the signature will be asymmetric and potentially unipolar. This is especially the case if only one 'hemisphere' of the structure is encountered (i.e. the planetward or tailward side). We direct the reader to diagrams in Borg et al. [2012] and DiBraccio et al. [2015] showing the effect trajectory can have on the magnetic signature of a plasmoid. The relative trajectories displayed are caused by a combination of the motion of the spacecraft and the current sheet. Differentiating between trajectories with large impact parameters and the travel-

139 ling compression regions that surround the plasmoids as they interact with the lobes [*Slavin*
140 *et al.*, 1993] will be accomplished using comparison to a model.

141 2.3 Force Free Model

142 The force free model represents a relatively stable configuration where no pressure gra-
143 dient is assumed to be present ($\nabla P = 0$). In this model the magnetic pressure ($B^2/2\mu_0$)
144 from the strong axial field is balanced by the magnetic tension force ($B^2/2\mu_0 R_c$), where μ_0
145 is the magnetic permeability of free space and R_c is the radius of curvature of the helical field.
146 This corresponds to the lowest energy state of helical magnetic fields, and is therefore perhaps
147 the end point of the evolution of the flux rope morphology [*Priest*, 1990]. Under these con-
148 ditions *Lepping et al.* [1990] showed that, using the *Lundquist* [1950] solutions, the field in-
149 side the flux rope can be written in cylindrical coordinates as:

$$150 B_{axial} = B_0 J_0(\alpha r') \quad (1)$$

$$152 B_{azimuthal} = B_0 H J_1(\alpha r') \quad (2)$$

$$154 B_r = 0 \quad (3)$$

155 where B_0 is the peak axial field strength, $J_0(\alpha r')$ and $J_1(\alpha r')$ are the zeroth and first-
156 order Bessel functions and H is the helicity or handedness of the flux rope ($H = \pm 1$). The
157 Bessel functions depend on the radial distance from the axis of the flux rope (r') and α . With
158 α set to 2.4048 [*Burlaga*, 1988], and setting the impact parameter: $r' = r/R_0$ (with R_0 be-
159 ing the radius of the flux rope) the model represents a flux rope with a completely axial field
160 at the center ($B_{azimuthal}(r = 0) = 0$) and an entirely azimuthal field at the edge ($(B_{axial}(r =$
161 $R_0) = 0)$). This formulation represents a cylindrically symmetric, linear (constant- α) force
162 free flux rope. The model has been successfully applied to interplanetary magnetic clouds [*Lep-*
163 *ping et al.*, 1990], FTEs at the magnetopause of Earth [*Eastwood et al.*, 2012a], Saturn [*Jasin-*
164 *ski et al.*, 2016] and Mercury [*Imber et al.*, 2014] as well as flux ropes in the magnetotails of
165 Earth [*Lepping et al.*, 1995, 1996; *Slavin et al.*, 2003a,b], Mars [*Eastwood et al.*, 2012b] and
166 Mercury [*DiBraccio et al.*, 2015].

167 The assumption that the flux rope is linearly (constant α) force free and cylindrically
168 symmetric will limit the number of flux ropes that are identified by the technique. As men-
169 tioned above, the model is likely to better represent well developed flux ropes. Flux ropes en-

170 countered soon after their formation are unlikely to have evolved to the stable equilibrium de-
171 scribed by the model. Implications of this assumption are discussed in Section 5.1.

172 3 Method

173 The technique, described below, uses three steps to locate quasi-force free flux ropes within
174 spacecraft magnetometer data. The combination of all three ensures fully automated, rigor-
175 ous and repeatable flux rope detections.

176 3.1 Baseline Crossing and Peak Detection

177 The aim of the first step in the technique is to find significant deflections in the B_Z com-
178 ponent of the field concurrent with peaks in the B_Y or $|B|$ components of the field. This field
179 signature is discussed in Section 2.2 as being the expected result of an equatorial magneto-
180 tail flux rope traveling sunward (or tailward) directly over the spacecraft.

181 This step is similar to the method developed by *Smith et al.* [2016] and is illustrated in
182 Figure 1. Once identified, candidates will be further analyzed and ultimately accepted or re-
183 jected based on the results of the subsequent steps. The algorithm first takes a running aver-
184 age of the B_Z component of the field within a one minute sliding window. The window size
185 was selected specifically for the Mercury data as it was found to trace the 'long' term changes
186 in the field but ignore sharp changes in the field (e.g. flux rope signatures). The running av-
187 erage forms a new baseline through which any deflections of the field must pass. Every in-
188 stance where B_Z passes through this baseline, henceforth referred to as a crossing, is recorded
189 for further analysis.

200 To investigate whether the deflection of the field is significant the method then searches
201 for local maxima and minima of B_Z . Defining the event using the local north-south maxima
202 of the field attempts to find the duration that would be chosen by eye, following the work of
203 *Slavin et al.* [1993], and more recently *Jackman et al.* [2014]; *Vogt et al.* [2014]; *DiBraccio et al.*
204 [2015]; *Smith et al.* [2016]. A period extending 1.25 s either side of the crossing (vertical gray
205 bars in Figure 1) is examined to find these local extrema. This time window was chosen in
206 order to preferentially select the fluctuations interpreted as flux ropes; *DiBraccio et al.* [2015]
207 reported an average duration of 0.74 s.

208 If the deflection is southward, i.e. the value of B_Z decreases, then all peaks in the field
209 (where the field is larger than at adjacent points) up to 1.25 s before the crossing are selected

210 as potential starts. On the other side, after the crossing, all local minima of the field (where
 211 the field is smaller or more negative than at adjacent points) up to 1.25 s after the crossing are
 212 selected as potential ends.

213 All possible combinations of potential starts and ends are then examined, with the aim
 214 of selecting the duration representing the largest and smoothest fluctuation. First order poly-
 215 nomials are interpolated between the various pairs. The interpolations are then compared with
 216 the data using the coefficient of determination, given by:

$$217 \quad r^2 = 1 - \frac{\sum_0^N (B_Z^t - f_t)^2}{\sum_0^N (B_Z^t - \bar{B}_Z)^2} \quad (4)$$

218 The start and end pair are located at $t = 0$ and $t = N$ respectively. B_Z^t is the value
 219 of B_Z at the point t , \bar{B}_Z is the average of B_Z over all points included. Finally, f_t is the value
 220 of the interpolation at time t . If all the data points lie precisely on the polynomial this would
 221 yield an r^2 value of 1. The grey, red and green lines on Figure 1 show the possible interpo-
 222 lations for the example event.

223 If the value of r^2 is less than 0.9 (e.g. as for the grey lines in Figure 1), and therefore
 224 the polynomial represents a poor fit to the data, then the start/end pair is discarded. The mag-
 225 nitude of the deflection, given by:

$$226 \quad \Delta B_Z = B_Z^0 - B_Z^N \quad (5)$$

227 is then evaluated for all pairs for which $0.9 \leq r^2 \leq 1$ (the green and red lines on Fig-
 228 ure 1) using Equation 5 (B_Z^0 and B_Z^N being the value of the B_Z component of the field at the
 229 start and end respectively). The start/end pair with the largest value of ΔB_Z is then selected,
 230 defining the event duration, shown by the green line in Figure 1. The method defines the lim-
 231 its of the event, shown by the vertical green bars in Figure 1. In this case the limits well match
 232 those that may have be selected by eye.

233 The magnitude of the deflection ($|\Delta B_Z|$) is then compared to the standard deviation of
 234 the field (σ_{B_Z}), requiring that:

$$235 \quad \frac{|\Delta B_Z|}{\sigma_{B_Z}} \geq 1 \quad (6)$$

236 where σ_{B_Z} is calculated for the same one minute sliding window as the average of B_Z .
 237 If Equation 6 is satisfied then the deflection is preliminarily accepted. This threshold is rel-
 238 atively low, however the aim of this step is to find all possible deflections so they may be eval-
 239 uated by the following methods.

240 The event duration identified is then inspected for local peaks in $B_{Y'}$ or $|B|$ using wavelet
 241 analysis. Figure 1 demonstrates this step. The green vertical bars indicate event duration as
 242 selected by the previous step. Panels c and f show the results of the Continuous Wavelet Trans-
 243 form (CWT) when applied to $|B_{Y'}|$ and $|B|$ (\sim panels b and e) respectively using the Ricker
 244 (or Mexican Hat/Marr) wavelet [Daubechies, 1992]. The Ricker wavelet is the normalized sec-
 245 ond derivative of a gaussian function, importantly featuring a central peak. The CWT and Ricker
 246 wavelet combination are commonly used in various fields for pattern matching and peak de-
 247 tection [Carmona et al., 1998; Du et al., 2006]. Panels c and f display time on the horizon-
 248 tal axis and wavelet scale on the vertical axis. The colors indicate the value of the CWT co-
 249 efficient, strongly positive where the wavelet (with a given scale) matches well with a peak
 250 in the data. Local peaks in the CWT coefficient are selected, and those greater than an em-
 251 pirical threshold (designed to preferentially select peaks with a small scale factor), are indi-
 252 cated with red stars. The red dashed lines then indicate the positions of these peaks in the panel
 253 of the corresponding component of the field.

254 If significant peaks are identified in either $B_{Y'}$ or $|B|$ (panels b or e) within the dura-
 255 tion indicated by the green and red bars then the deflection is accepted. Figure 1 shows an event
 256 for which peaks have been identified in both panels. However, only one peak is required as
 257 they can be missed by the CWT technique.

258 This combination of techniques recreates the by-eye selection criteria used by several
 259 previous studies [e.g. Slavin et al., 2003a; DiBraccio et al., 2015].

260 It is possible that the combination of B_Z deflection and peak in $B_{Y'}$ or $|B|$ could be
 261 caused by other magnetic structures within the magnetotail. To remove such signatures cri-
 262 teria are then placed on the results of both Minimum Variance Analysis (MVA) and compar-
 263 ison to a model (Sections 3.2 and 3.3).

3.2 Minimum Variance Analysis

The second stage of the process involves Minimum Variance Analysis (MVA); rotating the magnetic field data into a local coordinate system to further check for flux rope-like characteristics. If the magnetic signature is caused by a close encounter with a force-free flux rope then it may be expected that the new coordinate system is distinct and that a clear rotation of the field is apparent (as will be discussed below) [Slavin *et al.*, 1989; Briggs *et al.*, 2011; DiBraccio *et al.*, 2015].

MVA was first developed to find the normal to magnetic discontinuities (e.g. current layers) from magnetometer data [Sonnerup and Cahill, 1967]. However, the technique has also been used to determine the orientation and structure of flux ropes (if the spacecraft passes sufficiently close to the axis and the flux rope satisfies the force free approximation) [e.g. Sibeck *et al.*, 1984; Elphic *et al.*, 1986; Slavin *et al.*, 1989; Moldwin and Hughes, 1991; Xiao *et al.*, 2004].

MVA outputs three eigenvectors, representing the minimum, intermediate and maximum variation directions (\mathbf{e}_1 , \mathbf{e}_2 & \mathbf{e}_3 respectively), and three corresponding eigenvalues (λ_1 , λ_2 & λ_3). The three eigenvalues are often quoted in two ratios: the maximum to intermediate (λ_3/λ_2) and the intermediate to minimum (λ_2/λ_1). The relative size of the eigenvalues describes how well the new coordinate system is defined (low ratios suggest the axes are more degenerate [Khrabrov and Sonnerup, 1998; Sonnerup and Scheible, 1998]), so we require for event acceptance that both of the ratios are greater than five. Briggs *et al.* [2011], at Mars, placed a limit on λ_2/λ_1 of eight, while DiBraccio *et al.* [2015] placed no limits on either ratio and found λ_3/λ_2 as low as three, and λ_2/λ_1 always less than 12. DiBraccio *et al.* [2015] found that placing thresholds did not change their results and so chose to keep the larger sample for statistical reasons. For this study a threshold is used to help exclude poor quality events (as no manual pre-selection is performed). Requiring both ratios to be greater than 5 means all three eigenvectors are distinct. No criterion is placed upon the direction of the eigenvectors.

Additionally, the start and end times are varied (from those identified in Section 3.1) by $\pm 10\%$ of the duration. MVA is performed on all the possible combinations of starts and ends this allows. The amount by which the maximum eigenvalue ratio changes is then calculated by the following:

$$\max(\lambda_3/\lambda_2)/\min(\lambda_3/\lambda_2) \leq 1.75 \quad (7)$$

If the magnetic structure is well defined, and analysis stable, then the eigenvalue ratio should not change by a large amount, and Equation 7 should be satisfied. The limit of 1.75 was determined empirically from running the analysis on the ~ 10 test current sheet crossings

The pair for which the product of λ_3/λ_2 and λ_2/λ_1 is greatest is then selected, attempting to maximize both ratios (and thereby select the most distinct eigenvectors). Often this is the same as the duration selected in the previous step of the pipeline, or differs by only one data point.

Finally, a clear rotation of the field in a hodogram of the intermediate and maximum field directions is expected when the spacecraft passes through a flux rope. To evaluate this property an ellipse is fit using least squares minimization to the hodogram trace following the method of *Fitzgibbon et al.* [1999]. The quality of the fit to the data is evaluated using a modified r^2 (Equation 8):

$$r^2 = 1 - \frac{\sum_{i=0}^N a_i^2}{\sum_{i=0}^N c_i^2} \quad (8)$$

where the summations are over all data points ($i = 0$ to N), a_i is the radial distance between the point i and the ellipse (point P) and c_i is the radial distance between the center and the point P on the ellipse. If all points lie directly on the ellipse then $r^2 = 1$. We require that the fit is of a good quality: i.e. $r^2 \geq 0.98$. The ellipse fitting technique requires at least four data points; this imposes a lower limit to the duration of flux rope that can be identified depending on the resolution of the data used. With the 20 Hz MESSENGER data this is 0.2 s.

In addition, poor detections are characterized by highly eccentric ellipse fits, therefore for acceptance: $e \leq 0.9$. The ellipse fitting technique is known to have a bias for producing ellipses with low eccentricities [*Fitzgibbon et al.*, 1999]; therefore the fit should meet the criteria if possible.

Figure 2 show the results of running MVA on the flux rope shown in Figure 1. The expected flux rope characteristics can be seen; little variation in $B1$ (the minimum variance di-

rection), a peak (the core field) in $B2$ and an approximately bipolar signature in $B3$ (the maximum variance direction). If the spacecraft had passed through the center of the flux rope then $B1$ would be 0; $B1$ increases in magnitude as the impact parameter increases. The corresponding eigenvalue ratios are: $\lambda_3/\lambda_2 = 13.68$ and $\lambda_2/\lambda_1 = 7.22$, with a calculated variation in the maximum to intermediate ratio of 1.383. These values demonstrate a well defined MVA coordinate system with distinct eigenvectors. The ellipse in the $B2$ - $B3$ hodogram is a good fit ($r^2 = 0.996$) and is not highly eccentric ($e = 0.849$).

3.3 Force Free Flux Rope Fitting

The third and final step of the pipeline attempts to fit the data to a model flux rope. Not only does this provide another set of criteria to exclude poor quality signatures but also allows an estimation of the core field and proximity of the spacecraft to the flux rope axis. The implications of the choice of model are discussed in Section 5.1.

The aberrated magnetometer data, within the region identified in Section 3.2, is rotated into MVA coordinates and normalized. From there it is transformed into flux rope axial and azimuthal coordinates. The intermediate variance direction is taken to correspond to the axial direction while the azimuthal direction is composed of a combination of the minimum and maximum variance directions. This implicitly assumes that the MVA technique has correctly located the axial direction. This is a good assumption at small impact parameters, however it can be shown to become less valid as the impact parameter increases. Using the force free model an impact parameter of $0.5 R_0$ results in an angular difference between the intermediate direction and axial direction of $\sim 20^\circ$ [Xiao *et al.*, 2004].

The modeled magnetic field of the flux rope, shown in Equations 1 and 2, is normalized and computed for impact parameters between 0 and 0.95 (Impact Parameter = r/R_0). The results are then compared to the data using a modified χ^2 (χ_1^2), shown in Equation 9, as in DiBraccio *et al.* [2015]:

$$\chi_1^2 = \frac{\sum ((B_{Axial}^{Data} - B_{Axial}^{Model})^2 + (B_{Azimuthal}^{Data} - B_{Azimuthal}^{Model})^2)}{N} \quad (9)$$

where the sum is over all N data points, B_{Axial}^{Data} and $B_{Azimuthal}^{Data}$ are the normalized axial and azimuthal components of the field and B_{Axial}^{Model} and $B_{Azimuthal}^{Model}$ are the normalized axial and azimuthal results of the model. The model is compared to the MVA duration defined

in Section 3.2, however the fit is allowed to ignore up to the first and last 20% of the data points if this provides a better fit. This flexibility is somewhat analogous to *Slavin et al.* [2003a] allowing the time of closest approach to vary in their fitting. The impact parameter, and duration, with the smallest χ_1^2 is then selected as the best fit. For the flux rope in Figures 1 and 2 the best fit χ_1^2 (of 0.062) was obtained at an impact parameter of $0.33 R_0$.

Once the best fit to the normalized data has been computed the result is rotated back into MVA coordinates. Another measure of χ^2 is then evaluated comparing the three dimensional fit with the data; χ_2^2 is shown in Equation 10 (similar to that used by *Lepping et al.* [1990]):

$$\chi_2^2 = \frac{\sum ((B_1^{Data} - B_1^{Model})^2 + (B_2^{Data} - B_2^{Model})^2 + (B_3^{Data} - B_3^{Model})^2)}{3N - n} \quad (10)$$

where the sum is over all N data points; the differences between all three normalized minimum variance components of the field (as defined in Section 3.2) and the model results are calculated and squared. The factor of n here represents the number of free parameters in the fit (taken to be four). For the example flux rope (in Figures 1 and 2) the value of χ_2^2 calculated was 0.048. The peak axial field calculated by the model is then scaled to equal the peak axial field found in the MVA analysis to provide an estimate of B_0 : the core field strength. With the scaling completed the result can be rotated back into MSM coordinates.

With the data compared to the model results we place requirements both on the quality of the fit (χ^2) and the best fit impact parameter (IP). If the IP is larger than $0.5 R_0$ then the MVA technique should be less able to distinguish the axial orientation, and so the events are rejected. In addition we require that either χ_1^2 or χ_2^2 is less than 0.15 (so the flux rope can be well modeled as linearly force-free). Normally the two values of χ^2 are approximately the same.

4 Application

To test the efficacy of the method it has been applied to the same dataset as that previously investigated by *DiBraccio et al.* [2015]. During 30 MESSENGER magnetotail current sheet encounters, between 2011 and 2013, *DiBraccio et al.* [2015] identified a total of 49 flux ropes. The three step process independently re-identifies 8 of these. 19 of the flux ropes identified by *DiBraccio et al.* [2015] do not possess greater than 1σ deflections of the field in the B_Z component, and so are not located by the first step (though they do exhibit significant peaks

385 in B_Y and $|B|$). The remaining flux ropes that are not selected by the method are split evenly
 386 between those that did not meet the required MVA criteria and those that did not fit the force
 387 free model to the required accuracy (or did but for impact parameters $\geq 0.5 R_0$).

392 Figure 3 shows the result of the application of the method to two example passages of
 393 MESSENGER through the Hermean cross-tail current sheet on 23rd and 24th November 2011.
 394 The magnetic field is provided in aberrated MSM coordinates. The flux ropes identified by this
 395 method are shaded green. Those identified by *DiBraccio et al.* [2015] and missed by our method
 396 are highlighted in red. The top panel, showing data from the 23rd November 2011, was recorded
 397 during a period of high solar wind dynamic pressure (due to the impact of a coronal mass ejec-
 398 tion) [*Slavin et al.*, 2014]. This caused compression of the dayside magnetopause and very high
 399 rates of reconnection on the dayside. Correspondingly, a high rate of flux rope formation and
 400 ejection is observed. One flux rope identified by *DiBraccio et al.* [2015] is not recovered around
 401 09 : 25 : 40 due to a large variation in the MVA eigenvalues observed (violating the crite-
 402 rion in Equation 7). In the bottom panel a flux rope identified by *DiBraccio et al.* [2015] is
 403 not selected due to a large best fit impact parameter ($\geq 0.5 R_0$).

404 To further validate the technique it was applied to data from Earth's magnetotail: from
 405 the Cluster [*Escoubet et al.*, 1997; *Balogh et al.*, 2001; *Laakso et al.*, 2010] and Geotail [*Mukai*
 406 *et al.*, 1994] missions. The method was tested to check if it could recover events from the fig-
 407 ures of previous studies. Adapting it for the different timescales, the method identifies both
 408 flux ropes shown by *Slavin et al.* [2003a]. Three out of four flux ropes shown by *Borg et al.*
 409 [2012] are initially located, though two of these are then discarded as they do not fit the model
 410 satisfactorily at the required impact parameters. Both flux ropes shown by *Zhao et al.* [2016]
 411 are located, however one is later discarded as it does not sufficiently fit the model.

412 5 Discussion

413 The method described above represents an automated, consistent method of identifying
 414 *in-situ* encounters with cylindrically symmetric, linear (constant- α) flux ropes within space-
 415 craft magnetometer data. In the section below several key assumptions that the process makes
 416 are outlined and potential future adaptations are discussed.

417 5.1 Assumptions

418 The first major assumption made by the process is that the MVA process has correctly
419 determined the orientation of the flux rope. This has been shown in the past to be true in some
420 situations, and to be a better approximation when the spacecraft passes close to the axis [*Xiao*
421 *et al.*, 2004]. If MVA fails to correctly locate the axial direction then the event will appear to
422 be a poor fit to the model and the flux rope will probably not be identified.

423 Secondly, the force free model applied assumes that the flux rope is cylindrically sym-
424 metrical. It is probable that most flux ropes are in some way distorted through interactions with
425 the surrounding field and plasma. There are alternative models that allow for some deforma-
426 tion, for example those that allow an elliptical or oblate flux rope (e.g. *Hidalgo et al.* [2002]
427 and *Vandas and Romashets* [2003]). While these models allow more accurate fits of distorted
428 flux ropes they also introduce more free parameters. The purpose of the fit is to provide ad-
429 ditional criteria to rule out poor flux rope candidates and allow the estimation of some key pa-
430 rameters. More complex models could be subsequently fit to the successful candidate flux ropes
431 to discern more information about their structure.

432 Finally, the chosen model assumes that the flux rope is (constant- α) force free; this will
433 result in the exclusion of some flux ropes from the analysis. In fact, as mentioned in Section
434 2.5, the model is likely to be a poor fit to flux ropes that are encountered soon after their for-
435 mation. This will almost certainly introduce a selection effect. However, without access to high
436 resolution plasma data any model that includes the internal plasma pressure within a flux rope
437 would be poorly constrained. This could result in the inclusion of poor quality events if the
438 plasma parameters that are assumed are not representative of the true environment.

439 5.2 Adaptation

440 The analysis outlined above could be applied to other large data sets, and used to cre-
441 ate a self-consistent catalog of quasi-force free flux ropes. If used at other planets the times
442 scales used would require adjustment; i.e. the maximum length of event and duration over which
443 the averages are calculated. Additionally, if simultaneous high-resolution plasma data is avail-
444 able then this could be used to create additional criteria (or modify existing ones). Further-
445 more, such plasma data would also allow more complex analysis techniques to be employed
446 (e.g. the method of *Rong et al.* [2013] for determining axis orientation). Finally, the method

447 could be applied to virtual spacecraft simulation results, which can shed light on the limita-
448 tions of in-situ spacecraft detections.

449 **Conclusion**

450 We have presented a completely automated method of locating cylindrically symmet-
451 ric, linear (constant- α) flux ropes from spacecraft magnetometer data. The analysis initially
452 identifies significant ($\Delta B_z \geq 1\sigma$) deflections in the north-south component of the magnetic
453 field concurrent with peaks in the dawn-dusk component or total field. These candidates are
454 then inspected using MVA to select those for which it is able to determine a well defined co-
455 ordinate system with a clear rotation of the field. Those identified are then compared to a force
456 free model and the quality of the fit evaluated. The fitting of a model to the magnetic signa-
457 ture allows both the rejection of poor quality events (those likely due to other processes) and
458 the determination of some of the physical parameters of the flux rope (i.e. the radius of the
459 flux rope and core field strength). The pipeline has been tested on data from the MESSEN-
460 GER mission, and successfully re-locates several previously studied flux ropes from *DiBraz-
461 zo et al.* [2015]. It has also been applied to Earth data from Geotail and Cluster and recov-
462 ers some prominent examples from the literature [*Slavin et al.*, 2003a; *Borg et al.*, 2012; *Zhao
463 et al.*, 2016]. The method is ideal for application to large data sets whose manual inspection
464 would be time consuming and include unknown biases.

465 **Acknowledgments**

466 The data used in this study were available from the Planetary Data System (PDS): <http://pds.jpl.nasa.gov>.
467 AWS is funded by a SEPnet PhD studentship. CMJ is supported by STFC Ernest Rutherford
468 Fellowship number ST/L004399/1. RCF is supported by STFC Ernest Rutherford Fellowship
469 number ST/K004298/2. GAD is supported by a NASA Postdoctoral Program appointment at
470 the NASA Goddard Space Flight Center, administered by Universities Space Research Asso-
471 ciation through a contract with NASA. LT is supported by STFC Ernest Rutherford grant ST/L002809/1.
472 Cluster data used in this paper were downloaded from the European Space Agency's Cluster
473 and Double Star Science Archive (<http://www.cosmos.esa.int/web/csa/access>). Geotail mag-
474 netic field (electric field and/or plasma) data were provided by T. Nagai (H. Hayakawa and/or
475 Y. Saito) through DARTS at Institute of Space and Astronautical Science, JAXA in Japan.

References

- 476
477 Akasofu, S.-I. (1964), The development of the auroral substorm, *Planetary and Space*
478 *Science*, *12*(4), 273–282, doi:[http://dx.doi.org/10.1016/0032-0633\(64\)90151-5](http://dx.doi.org/10.1016/0032-0633(64)90151-5).
- 479 Anderson, B., M. Acuña, D. Lohr, J. Scheifele, A. Raval, H. Korth, and J. Slavin (2007),
480 The Magnetometer Instrument on MESSENGER, *Space Science Reviews*, *131*(1-4),
481 147–150, doi:10.1007/s11214-007-9246-7.
- 482 Anderson, B. J., C. L. Johnson, H. Korth, M. E. Purucker, R. M. Winslow, J. A. Slavin,
483 S. C. Solomon, R. L. McNutt, J. M. Raines, and T. H. Zurbuchen (2011), The Global
484 Magnetic Field of Mercury from MESSENGER Orbital Observations, *Science*,
485 *333*(6051), 1859–1862, doi:10.1126/science.1211001.
- 486 Baker, D. N., T. I. Pulkkinen, V. Angelopoulos, W. Baumjohann, and R. L. McPherron
487 (1996), Neutral line model of substorms: Past results and present view, *Journal of*
488 *Geophysical Research: Space Physics*, *101*(A6), 12,975–13,010, doi:10.1029/95JA03753.
- 489 Balogh, A., C. M. Carr, M. H. Acuña, M. W. Dunlop, T. J. Beek, P. Brown, K.-H.
490 Tomacon, E. Georgescu, K.-H. Glassmeier, J. Harris, G. Musmann, T. Oddy, and
491 K. Schwingenschuh (2001), The Cluster Magnetic Field Investigation: overview of
492 in-flight performance and initial results, *Annales Geophysicae*, *19*(10/12), 1207–1217,
493 doi:10.5194/angeo-19-1207-2001.
- 494 Borg, M. L., M. Taylor, and J. P. Eastwood (2012), Observations of magnetic flux ropes
495 during magnetic reconnection in the Earth's magnetotail, *Annales Geophysicae*, *30*(5),
496 761–773.
- 497 Briggs, J. A., D. A. Brain, M. L. Cartwright, J. P. Eastwood, and J. S. Halekas (2011),
498 A statistical study of flux ropes in the Martian magnetosphere, *Planetary and Space*
499 *Science*, *59*(13), 1498–1505, doi:<http://dx.doi.org/10.1016/j.pss.2011.06.010>.
- 500 Dalgarno, L. F. (1988), Magnetic clouds and force-free fields with constant al-
501 pha, *Journal of Geophysical Research: Space Physics*, *93*(A7), 7217–7224, doi:
502 [10.1029/JA093iA07p07217](https://doi.org/10.1029/JA093iA07p07217).
- 503 Carmona, R., W. L. Hwang, and B. Torresani (1998), *Practical Time-Frequency Analysis:*
504 *Gabor and Wavelet Transforms, with an Implementation in S, Wavelet Analysis and Its*
505 *Applications*, Elsevier Science.
- 506 Cowley, S. W. H. (1981), Magnetospheric asymmetries associated with the y-component
507 of the IMF, *Space Science Reviews*, *29*, 79–96.
- 508 Daubechies, I. (1992), *Ten lectures on wavelets*, vol. 61, SIAM.

- 509 DiBraccio, G. A., J. A. Slavin, S. M. Imber, D. J. Gershman, J. M. Raines,
510 C. M. Jackman, S. A. Boardsen, B. J. Anderson, H. Korth, T. H. Zurbuchen,
511 R. L. M. Jr., and S. C. Solomon (2015), MESSENGER observations of flux
512 ropes in Mercury's magnetotail, *Planetary and Space Science*, *115*, 77–89, doi:
513 <http://dx.doi.org/10.1016/j.pss.2014.12.016>.
- 514 Du, P., W. A. Kibbe, and S. M. Lin (2006), Improved peak detection in mass spectrum
515 by incorporating continuous wavelet transform-based pattern matching, *Bioinformatics*,
516 *22(17)*, 2059–2065, doi:10.1093/bioinformatics/btl355.
- 517 Dungey, J. W. (1961), Interplanetary Magnetic Field and the Auroral Zones, *Phys. Rev.*
518 *Let.*, *6*, 47–48.
- 519 Eastwood, J. P., T. D. Phan, R. C. Fear, D. G. Sibeck, V. Angelopoulos, M. Øieroset, and
520 M. Shay (2012a), Survival of flux transfer event (FTE) flux ropes far along the tail
521 magnetopause, *Journal of Geophysical Research: Space Physics*, *117*(A8), n/a—n/a,
522 doi:10.1029/2012JA017722.
- 523 Eastwood, J. P., J. J. H. Videira, D. A. Brain, and J. S. Halekas (2012b), A chain of
524 magnetic flux ropes in the magnetotail of Mars, *Geophysical Research Letters*, *39*(3),
525 n/a—n/a, doi:10.1029/2011GL050444.
- 526 Elphic, R. C., C. A. Cattell, K. Takahashi, S. J. Bame, and C. T. Russell (1986), ISEE-
527 1 and 2 observations of magnetic flux ropes in the magnetotail: FTE's in the plasma
528 sheet?, *Geophysical Research Letters*, *13*(7), 648–651, doi:10.1029/GL013i007p00648.
- 529 Escoubet, C. P., R. Schmidt, and M. L. Goldstein (1997), Cluster — Science and Mission
530 Overview, in *Space Science Reviews*, vol. 79, edited by P. Escoubet, C., R. Schmidt, and
531 C. T. Russell, 1 ed., pp. 11–32, Springer Netherlands, doi:10.1023/A:1004923124586.
- 532 Fitzgibbon, A., M. Pilu, and R. B. Fisher (1999), Direct Least Squares Fitting of Ellipses,
533 *IEEE Transactions On Pattern Analysis and Machine Intelligence*, *21*(5), 476–480.
- 534 Hidalgo, M. A., T. Nieves-Chinchilla, and C. Cid (2002), Elliptical cross-section model
535 for the magnetic topology of magnetic clouds, *Geophysical Research Letters*, *29*(13),
536 14–15, doi:10.1029/2001GL013875.
- 537 Huang, C.-S. (2002), Evidence of periodic (2–3 hour) near-tail magnetic reconnection and
538 plasmoid formation: Geotail observations, *Geophysical Research Letters*, *29*(24), 42–44,
539 doi:10.1029/2002GL016162.
- 540 Hughes, W. J., and D. G. Sibeck (1987), On the 3-dimensional structure of plasmoids,
541 *Geophysical Research Letters*, *14*(6), 636–639, doi:10.1029/GL014i006p00636.

- 542 Ieda, A., S. Machida, T. Mukai, Y. Saito, T. Yamamoto, A. Nishida, T. Terasawa, and
543 S. Kokubun (1998), Statistical analysis of the plasmoid evolution with Geotail ob-
544 servations, *Journal of Geophysical Research: Space Physics*, *103*(A3), 4453–4465,
545 doi:10.1029/97JA03240.
- 546 Imber, S. M., J. A. Slavin, S. A. Boardsen, B. J. Anderson, H. Korth, R. L. McNutt, and
547 S. C. Solomon (2014), MESSENGER observations of large dayside flux transfer events:
548 Do they drive Mercury’s substorm cycle?, *Journal of Geophysical Research: Space*
549 *Physics*, *119*(7), 5613–5623, doi:10.1002/2014JA019884.
- 550 Jackman, C. M., J. A. Slavin, M. G. Kivelson, D. J. Southwood, N. Achilleos, M. F.
551 Thomsen, G. A. DiBraccio, J. P. Eastwood, M. P. Freeman, M. K. Dougherty, and
552 M. F. Vogt (2014), Saturn’s dynamic magnetotail: A comprehensive magnetic field and
553 plasma survey of plasmoids and traveling compression regions and their role in global
554 magnetospheric dynamics, *Journal of Geophysical Research-Space Physics*, *119*(7),
555 5465–5494.
- 556 Jasinski, J. M., J. A. Slavin, C. S. Arridge, G. Poh, X. Jia, N. Sergis, A. J. Coates,
557 G. H. Jones, and J. Hunter Waite (2016), Flux Transfer Event observation at Sat-
558 urn’s dayside magnetopause by the Cassini spacecraft, *Geophysical Research Letters*,
559 doi:10.1002/2016GL069260.
- 560 Karimabadi, H., T. B. Sipes, H. White, M. Marinucci, A. Dmitriev, J. K. Chao, J. Driscoll,
561 and N. Balac (2007), Data mining in space physics: MineTool algorithm, *Journal of*
562 *Geophysical Research-Space Physics*, *112*(A11), 11.
- 563 Karimabadi, H., T. B. Sipes, Y. Wang, B. Lavraud, and A. Roberts (2009), A new multi-
564 variable time series data analysis technique: Automated detection of flux transfer events
565 using Cluster data, *Journal of Geophysical Research-Space Physics*, *114*, 13.
- 566 Kawano, H., and C. T. Russell (1996), Survey of flux transfer events observed with the
567 ISEE 1 spacecraft: Rotational polarity and the source region, *Journal of Geophysical*
568 *Research: Space Physics*, *101*(A12), 27,299–27,308, doi:10.1029/96JA02703.
- 569 Khabarov, A. V., and B. U. Ö. Sonnerup (1998), Error estimates for minimum variance
570 analysis, *Journal of Geophysical Research: Space Physics*, *103*(A4), 6641–6651, doi:
571 10.1029/97JA03731.
- 572 Laakso, H., C. Perry, S. McCaffrey, D. Herment, A. Allen, C. Harvey, P. Escoubet,
573 C., C. Gruenberger, M. Taylor, and R. Turner (2010), The Cluster Active Archive:
574 Overview, in *The Cluster Active Archive*, edited by H. Laakso, M. Taylor, and P. Escou-

- 575 bet, C., 1 ed., pp. 3–37, Springer Netherlands, doi:10.1007/978-90-481-3499-1.
- 576 Lepping, R. P., J. A. Jones, and L. F. Burlaga (1990), Magnetic field structure of inter-
577 planetary magnetic clouds at 1 AU, *Journal of Geophysical Research: Space Physics*,
578 95(A8), 11,957–11,965.
- 579 Lepping, R. P., D. H. Fairfield, J. Jones, L. A. Frank, W. R. Paterson, S. Kokubun, and
580 T. Yamamoto (1995), Cross-tail magnetic flux ropes as observed by the GEOTAIL
581 spacecraft, *Geophysical Research Letters*, 22(10), 1193–1196, doi:10.1029/94GL01114.
- 582 Lepping, R. P., J. A. Slavin, M. Hesse, J. A. Jones, and A. Szabo (1996), Analysis of
583 Magnetotail Flux Ropes with Strong Core Fields: ISEE 3 Observations, *Journal of*
584 *Geomagnetism and Geoelectricity*, 48(5), 589–601.
- 585 Lundquist, S. (1950), Magnetohydrostatic Fields, *Ark. Fys*, 2, 361–365.
- 586 Malaspina, D. M., and J. T. Gosling (2012), Two spacecraft observations of magnetic dis-
587 continuities in the solar wind with STEREO, *Journal of Geophysical Research: Space*
588 *Physics*, 117(A4), n/a—n/a, doi:10.1029/2011JA017375.
- 589 Moldwin, M. B., and W. J. Hughes (1991), Plasmoids as magnetic flux ropes, *Journal of*
590 *Geophysical Research: Space Physics*, 96(A8), 14,051–14,064, doi:10.1029/91JA01167.
- 591 Moldwin, M. B., and W. J. Hughes (1992), On the Formation and Evolution of Plas-
592 moids: A Survey of ISEE 3 Geotail Data, *J. Geophys. Res.*, 97(A12), 19,259–19,282,
593 doi:10.1029/92ja01598.
- 594 Machida, T., S. Machida, Y. Saito, M. Hirahara, T. Terasawa, N. Kaya, T. Obara, M. Ejiri,
595 and A. Nishida (1994), The Low Energy Particle (LEP) Experiment onboard the
596 GEOTAIL Satellite, *Journal of geomagnetism and geoelectricity*, 46(8), 669–692, doi:
597 10.5636/jgg.46.669.
- 598 Priest, E. R. (1990), The Equilibrium of Magnetic Flux Ropes, *Geophys. Monogr.*, 58,
599 1–22.
- 600 Richardson, I. G., S. W. H. Cowley, E. W. Hones, and S. J. Bame (1987), PLASMOID-
601 ASSOCIATED ENERGETIC ION BURSTS IN THE DEEP GEOMAGNETIC TAIL
602 - PROPERTIES OF PLASMOIDS AND THE POSTPLASMOID PLASMA SHEET,
603 *Journal of Geophysical Research-Space Physics*, 92(A9), 9997–10,013.
- 604 Rong, Z. J., W. X. Wan, C. Shen, T. L. Zhang, A. T. Y. Lui, Y. Wang, M. W. Dunlop,
605 Y. C. Zhang, and Q. G. Zong (2013), Method for inferring the axis orientation of cylin-
606 drical magnetic flux rope based on single-point measurement, *Journal of Geophysical*
607 *Research: Space Physics*, 118(1), 271–283, doi:10.1029/2012JA018079.

- 608 Schindler, K. (1974), A theory of the substorm mechanism, *Journal of Geophysical Re-*
609 *search*, 79(19), 2803, doi:10.1029/JA079i019p02803.
- 610 Scholer, M., G. Gloeckler, D. Hovestadt, B. Klecker, and F. M. Ipavich (1984), Charac-
611 teristics of plasmoidlike structures in the distant magnetotail, *Journal of Geophysical*
612 *Research*, 89(A10), 8872, doi:10.1029/JA089iA10p08872.
- 613 Sibeck, D. G., G. L. Siscoe, J. A. Slavin, E. J. Smith, S. J. Bame, and F. L. Scarf
614 (1984), Magnetotail flux ropes, *Geophysical Research Letters*, 11(10), 1090–1093,
615 doi:10.1029/GL011i010p01090.
- 616 Siscoe, G. L., N. F. Ness, and C. M. Yeates (1975), Substorms on Mercury?, *Journal of*
617 *Geophysical Research*, 80(31), 4359–4363, doi:10.1029/JA080i031p04359.
- 618 Slavin, J. A., D. N. Baker, J. D. Craven, R. C. Elphic, D. H. Fairfield, L. A. Frank, A. B.
619 Galvin, W. J. Hughes, R. H. Manka, D. G. Mitchell, I. G. Richardson, T. R. Sanderson,
620 D. J. Sibeck, E. J. Smith, and R. D. Zwickl (1989), CDAW 8 observations of plasmoid
621 signatures in the geomagnetic tail: An assessment, *Journal of Geophysical Research:*
622 *Space Physics*, 94(A11), 15,153–15,175, doi:10.1029/JA094iA11p15153.
- 623 Slavin, J. A., M. F. Smith, E. L. Mazur, D. N. Baker, E. W. Hones, T. Iyemori, and E. W.
624 Hovestadt (1993), ISEE 3 observations of traveling compression regions in the Earth's
625 magnetotail, *Journal of Geophysical Research: Space Physics*, 98(A9), 15,425–15,446.
- 626 Slavin, J. A., R. P. Lepping, J. Gjerloev, D. H. Fairfield, M. Hesse, C. J. Owen, M. B.
627 Moldwin, T. Nagai, A. Ieda, and T. Mukai (2003a), Geotail observations of mag-
628 netic flux ropes in the plasma sheet, *Journal of Geophysical Research-Space Physics*,
629 108(A1), 18.
- 630 Slavin, J. A., R. P. Lepping, J. Gjerloev, M. L. Goldstein, D. H. Fairfield, M. H. Acuna,
631 A. Balogh, M. Dunlop, M. G. Kivelson, K. Khurana, A. Fazakerley, C. J. Owen,
632 H. Reme, and J. M. Bosqued (2003b), Cluster electric current density measurements
633 within a magnetic flux rope in the plasma sheet, *Geophysical Research Letters*, 30(7), 4.
- 634 Slavin, J. A., M. H. Acuna, B. J. Anderson, D. N. Baker, M. Benna, S. A. Boardsen,
635 G. Gloeckler, R. E. Gold, G. C. Ho, H. Korth, S. M. Krimigis, R. L. McNutt Jr., J. M.
636 Raines, M. Sarantos, D. Schriver, S. C. Solomon, P. Travnicek, and T. H. Zurbuchen
637 (2009), MESSENGER Observations of Magnetic Reconnection in Mercury's Magneto-
638 sphere, *SCIENCE*, 324(5927), 606–610.
- 639 Slavin, J. A., B. J. Anderson, D. N. Baker, M. Benna, S. A. Boardsen, G. Gloeckler, R. E.
640 Gold, G. C. Ho, H. Korth, S. M. Krimigis, R. L. McNutt, L. R. Nittler, J. M. Raines,

- 641 M. Sarantos, D. Schriver, S. C. Solomon, R. D. Starr, P. M. Trávníček, and T. H. Zurbuchen (2010), MESSENGER Observations of Extreme Loading and Unloading of
642 Mercury's Magnetic Tail, *Science*, 329(5992), 665–668, doi:10.1126/science.1188067.
- 643
644 Slavin, J. A., B. J. Anderson, D. N. Baker, M. Benna, S. A. Boardsen, R. E. Gold, G. C.
645 Ho, S. M. Imber, H. Korth, S. M. Krimigis, R. L. McNutt, J. M. Raines, M. Sarantos,
646 D. Schriver, S. C. Solomon, P. Trávníček, and T. H. Zurbuchen (2012), MESSEN-
647 GER and Mariner 10 flyby observations of magnetotail structure and dynamics at
648 Mercury, *Journal of Geophysical Research: Space Physics*, 117(A1), n/a—n/a, doi:
649 10.1029/2011JA016900.
- 650 Slavin, J. A., G. A. DiBraccio, D. J. Gershman, S. M. Imber, G. K. Poh, J. M. Raines,
651 T. H. Zurbuchen, X. Jia, D. N. Baker, K.-H. Glassmeier, S. A. Livi, S. A. Boardsen,
652 T. A. Cassidy, M. Sarantos, T. Sundberg, A. Masters, C. L. Johnson, R. M. Winslow,
653 B. J. Anderson, H. Korth, R. L. McNutt, and S. C. Solomon (2014), MESSENGER
654 observations of Mercury's dayside magnetosphere under extreme solar wind con-
655 ditions, *Journal of Geophysical Research: Space Physics*, 119(10), 8087–8116, doi:
656 10.1002/2014JA020319.
- 657 Smith, A. W., C. M. Jackman, and M. F. Thomsen (2016), Magnetic Reconnection in
658 Saturn's Magnetotail: A Comprehensive Magnetic Field Survey, *Journal of Geophysical*
659 *Research: Space Physics*, pp. n/a–n/a, doi:10.1002/2015JA022005.
- 660 Solomon, S. C., R. L. McNutt Jr, R. E. Gold, and D. L. Domingue (2007), MESSENGER
661 mission overview, *Space Science Reviews*, 131(1-4), 3–39.
- 662 Sonnerup, B. U. Ö., and L. J. Cahill (1967), Magnetopause structure and attitude from
663 Explorer 12 observations, *Journal of Geophysical Research*, 72(1), 171–183, doi:
664 10.1029/JZ072i001p00171.
- 665 Sonnerup, B. U. Ö., and M. Scheible (1998), Minimum and maximum variance analysis,
666 in *Analysis Methods for Multi-Spacecraft Data*, edited by G. Paschmann and P. W. Daly,
667 pp. 185–220, ISSI Scientific Report SR-001, ISSI/ESA.
- 668 Sun, W.-J., J. A. Slavin, S. Fu, J. M. Raines, Q.-G. Zong, S. M. Imber, Q. Shi, Z. Yao,
669 C. Poh, D. J. Gershman, Z. Pu, T. Sundberg, B. J. Anderson, H. Korth, and D. N.
670 Baker (2015), MESSENGER observations of magnetospheric substorm activity in
671 Mercury's near magnetotail, *Geophysical Research Letters*, 42(10), 3692–3699, doi:
672 10.1002/2015GL064052.

- 673 Vandas, M., and E. P. Romashets (2003), A force-free field with constant alpha in an
674 oblate cylinder: A generalization of the Lundquist solution, *Astronomy and Astrophysics*,
675 398(3), 801–807.
- 676 Vasquez, B. J., V. I. Abramenko, D. K. Haggerty, and C. W. Smith (2007), Numerous
677 small magnetic field discontinuities of Bartels rotation 2286 and the potential role of
678 Alfvénic turbulence, *Journal of Geophysical Research: Space Physics*, 112(A11), n/a–
679 n/a, doi:10.1029/2007JA012504.
- 680 Vogt, M. F., M. G. Kivelson, K. K. Khurana, S. P. Joy, and R. J. Walker (2010), Recon-
681 nection and flows in the Jovian magnetotail as inferred from magnetometer observa-
682 tions, *Journal of Geophysical Research-Space Physics*, 115, 19.
- 683 Vogt, M. F., C. M. Jackman, J. A. Slavin, E. J. Bunce, S. W. H. Cowley, M. G. Kivelson,
684 and K. K. Khurana (2014), Structure and statistical properties of plasmoids in Jupiter’s
685 magnetotail, *Journal of Geophysical Research-Space Physics*, 119(2), 821–843.
- 686 Xiao, C. J., Z. Y. Pu, Z. W. Ma, S. Y. Fu, Z. Y. Huang, and Q. G. Zong (2004), Infer-
687 ring of flux rope orientation with the minimum variance analysis technique, *Journal of*
688 *Geophysical Research: Space Physics*, 109(A11), n/a—n/a, doi:10.1029/2004JA010594.
- 689 Zhao, Y., R. Wang, and A. Du (2016), Characteristics of field-aligned currents associated
690 with magnetic flux ropes in the magnetotail: A statistical study, *Journal of Geophysical*
691 *Research: Space Physics*, pp. n/a–n/a, doi:10.1002/2015JA022144.



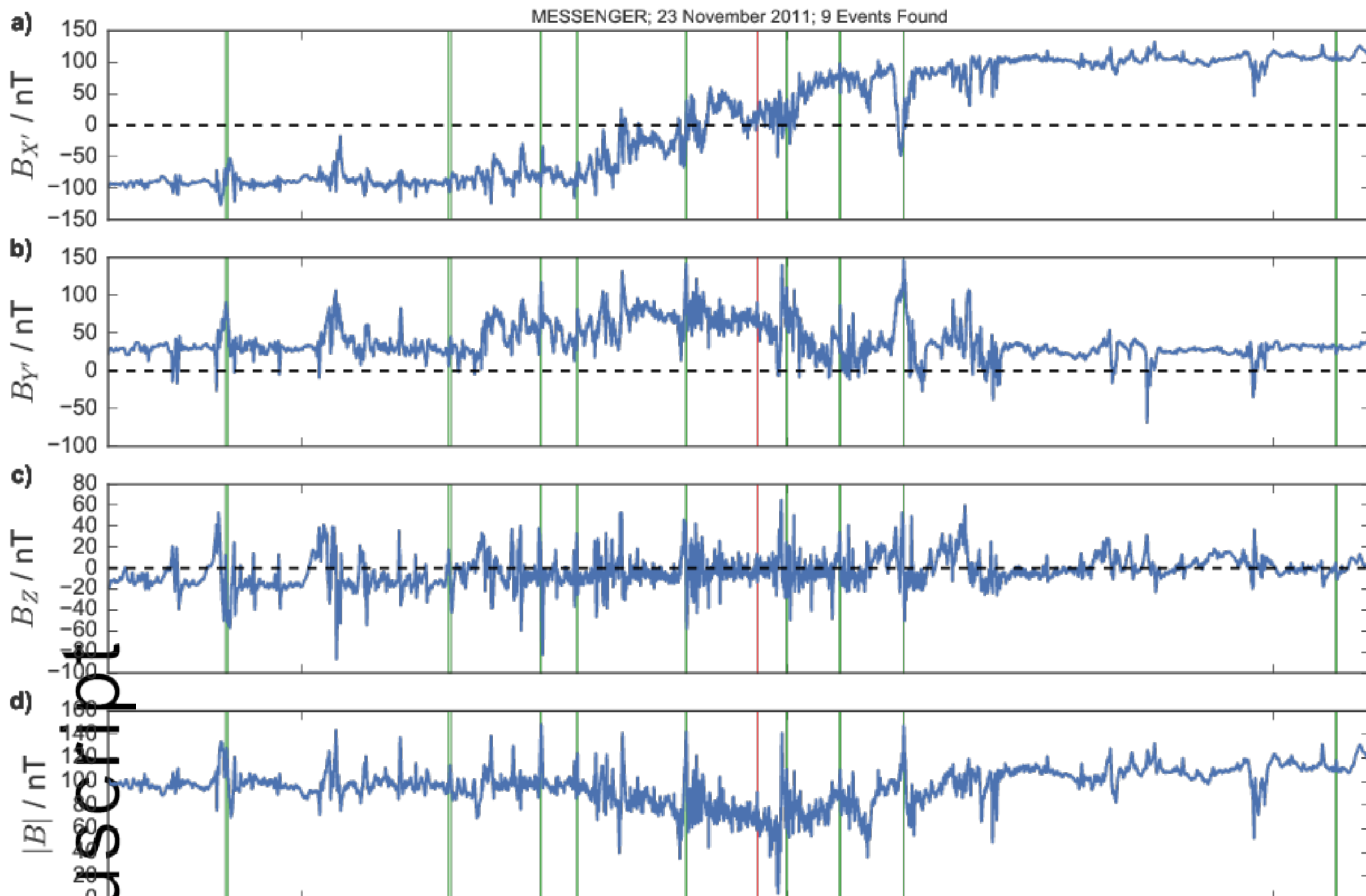
190 **Figure 1.** An example flux rope detection. Panels a, b, d and e show the magnetic field in aberrated MSM
 191 coordinates. The grey vertical bars on panel d indicate the maximum length of the event (± 1.25 s). The faint
 192 grey lines show the first order polynomials interpolated between the potential start/stop pairings that have a
 193 value of $r^2 < 0.9$. The red lines indicate those interpolated lines with an $r^2 \geq 0.9$ (calculated from Equation
 194 4). The green line shows the final interpolated line selected; with an $r^2 \geq 0.9$ and the largest value of ΔB_Z
 195 (from Equation 5). The green vertical lines indicate the corresponding selected start and end to the deflection
 196 respectively. Panels c and f show the Continuous Wavelet Transform (CWT) of $|B_{Y'}|$ and $|B|$ respectively
 197 (with the Ricker wavelet). The color bar indicates the value of the CWT coefficient, while the vertical axis
 198 shows the wavelet scale factor. The red stars indicate the locations of the significant peaks in the CWT. The
 199 red dashed lines then show the locations of the peaks in the panel of the relevant magnetic field component.



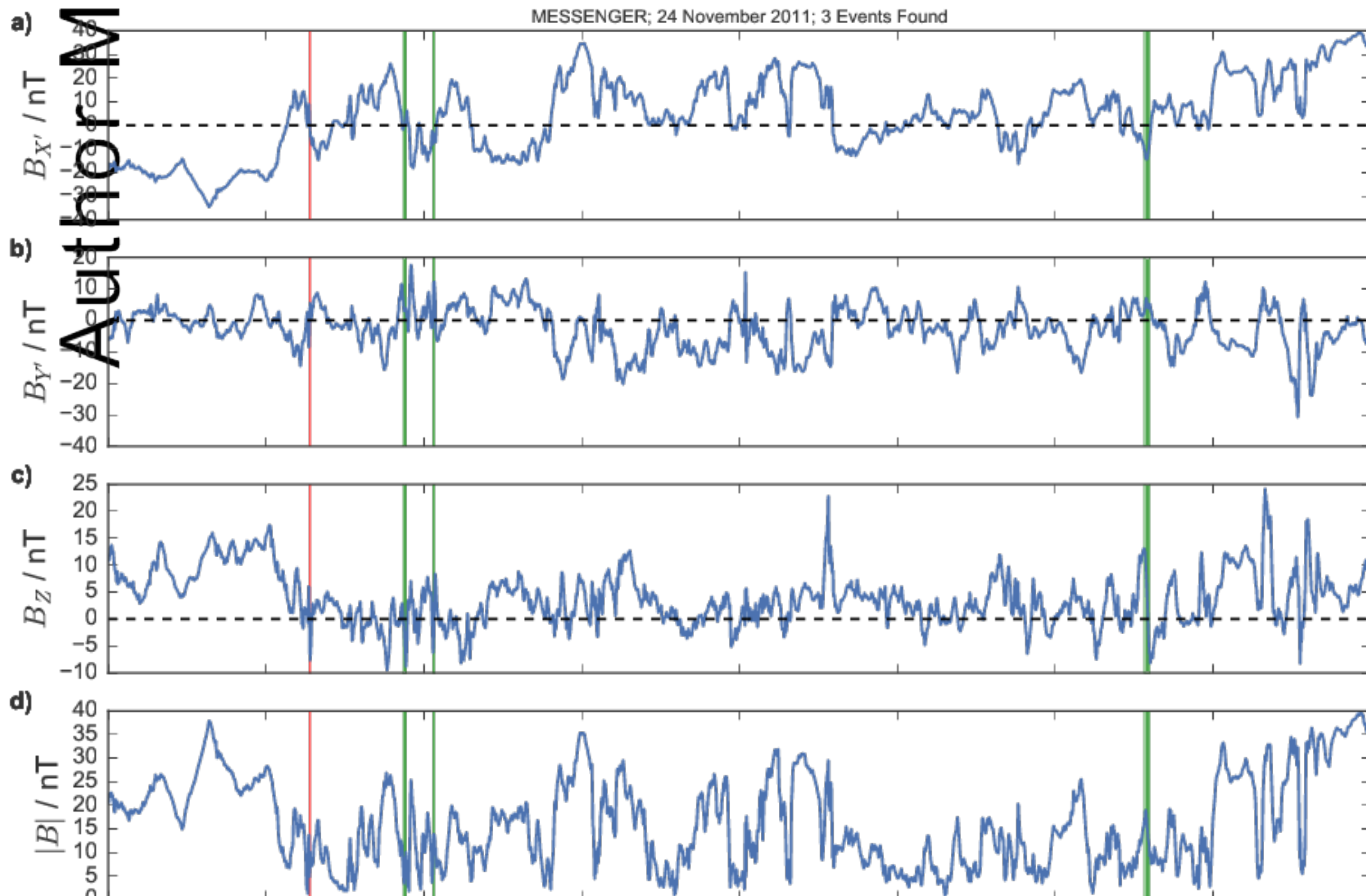
277 **Figure 2.** Results of the MVA analysis on the example flux rope shown in Figures 1 and 2. The magnetic
278 field is shown in the MVA coordinate system, where B1, B2 and B3 are the field components in the minimum,
279 intermediate and maximum variance directions respectively. Hodograms of the field are also shown. The
280 hodogram displaying B2-B3 (panel f) is over-plotted with the result of the ellipse fitting in green (described in
281 Section 3.2); the green dot is the center of the fitted ellipse.



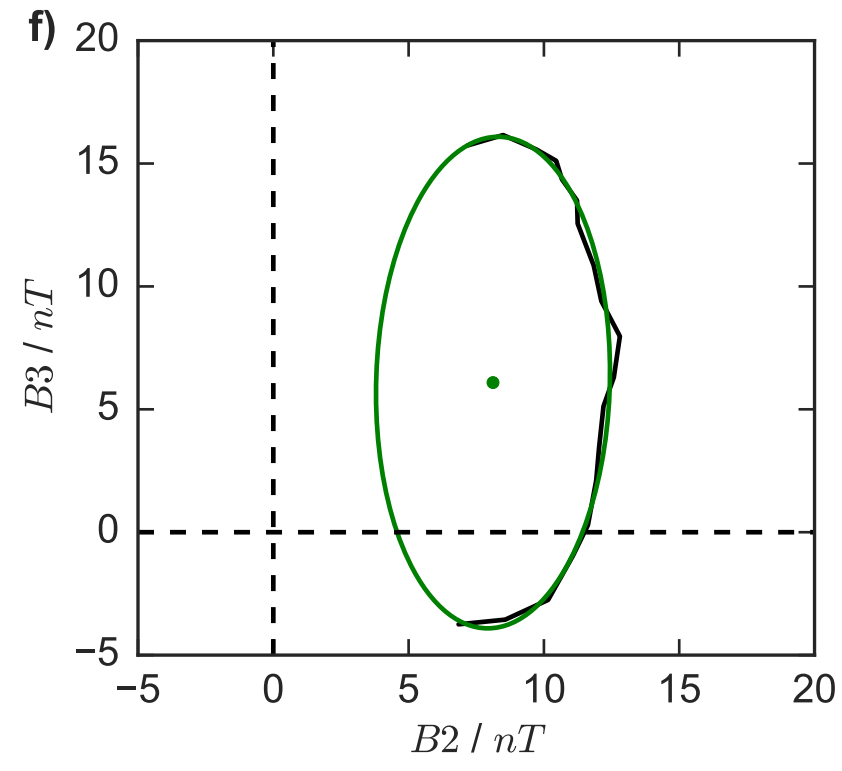
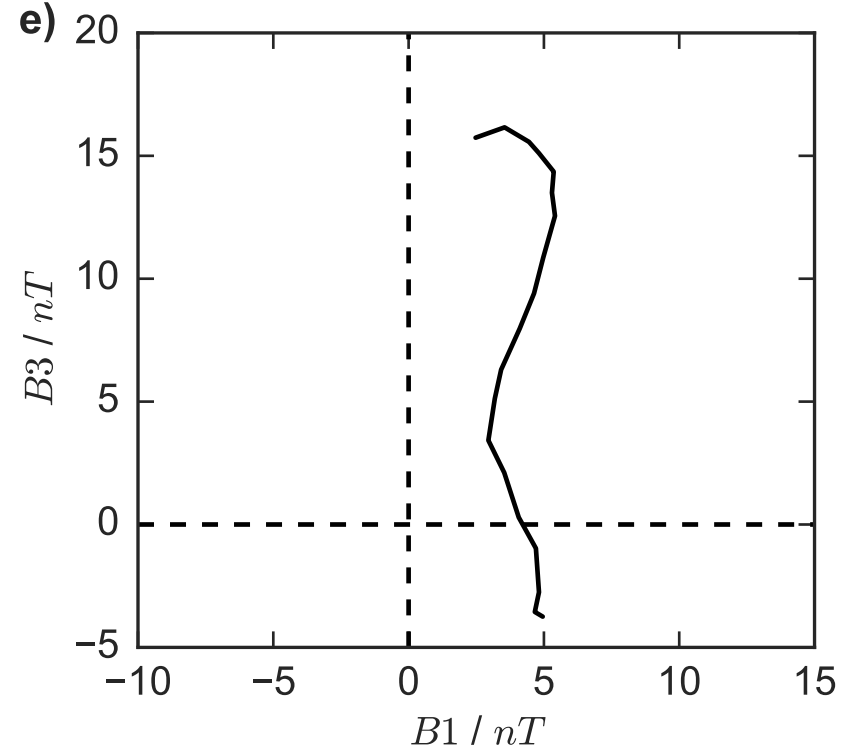
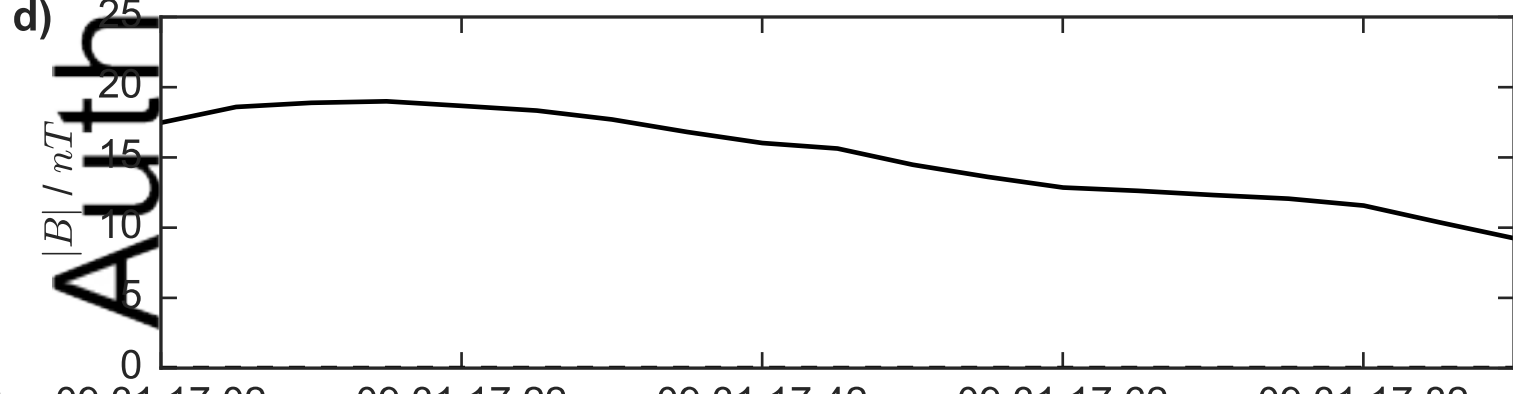
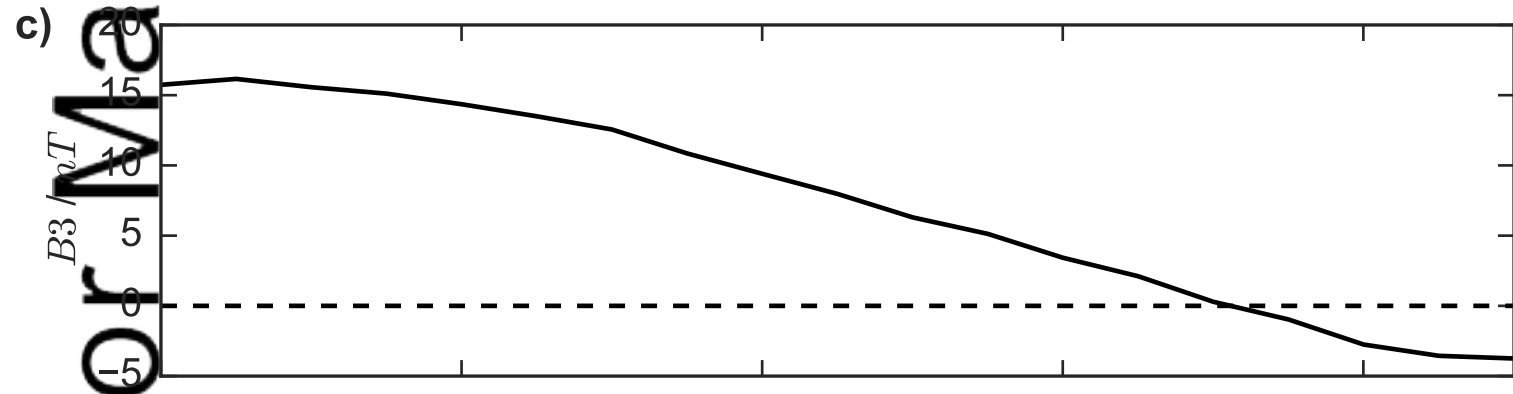
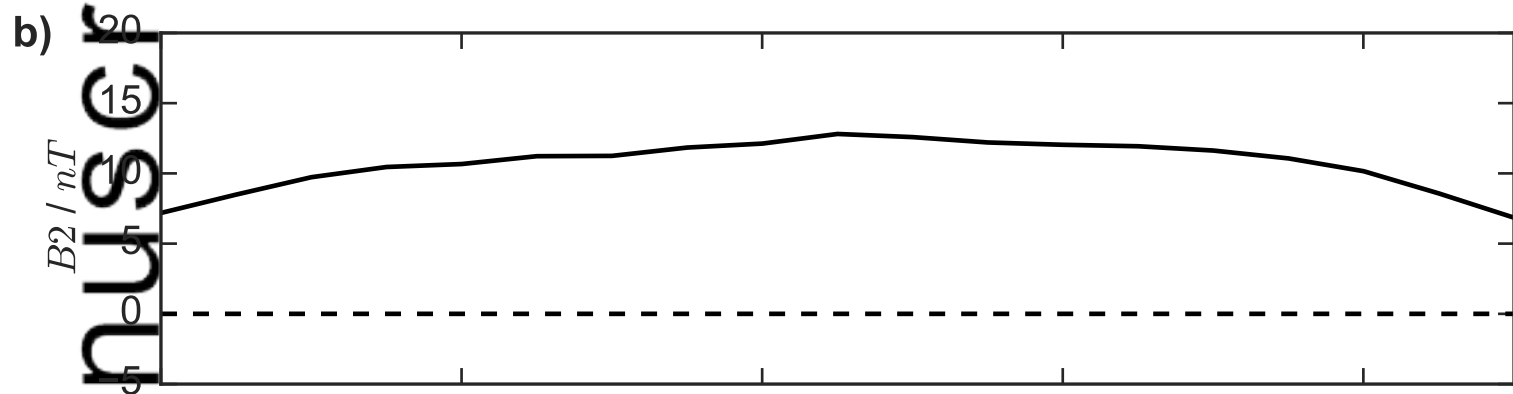
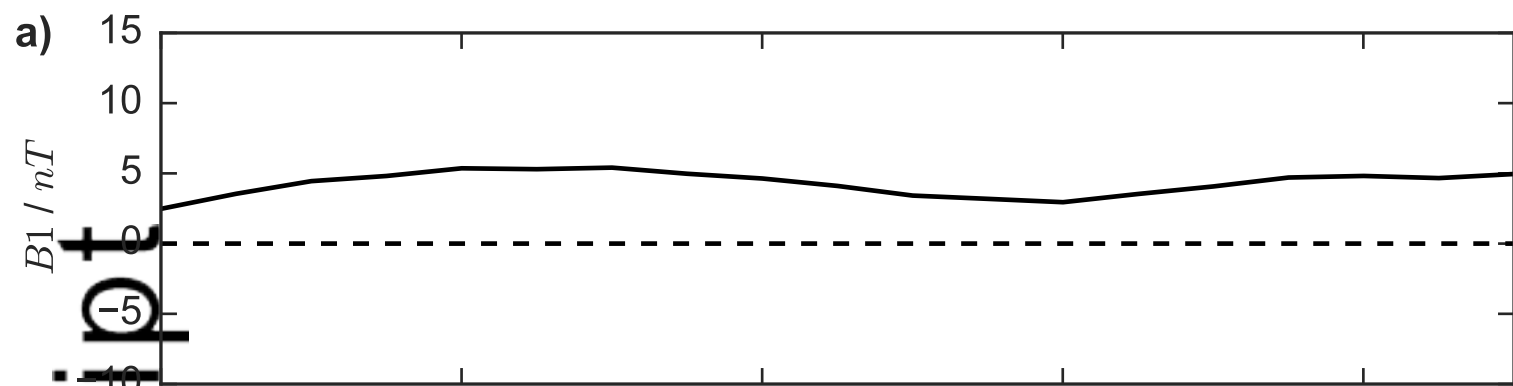
388 **Figure 3** Two example MESSENGER passages through the Hermean magnetotail current sheet. Magnetic
389 field is provided in aberrated MSM coordinates. Positive force free flux rope detections by the method are
390 indicated with green shading. Flux ropes identified by *DiBraccio et al.* [2015] but missed by this technique
391 are highlighted in red.



Time (UT)	09:21:00	09:26:00	09:31:00
$X'_{MSM} (R_M)$	-2.75	-2.57	-2.38
$Y'_{MSM} (R_M)$	0.19	0.15	0.12
$Z_{MSM} (R_M)$	-0.28	-0.09	0.10



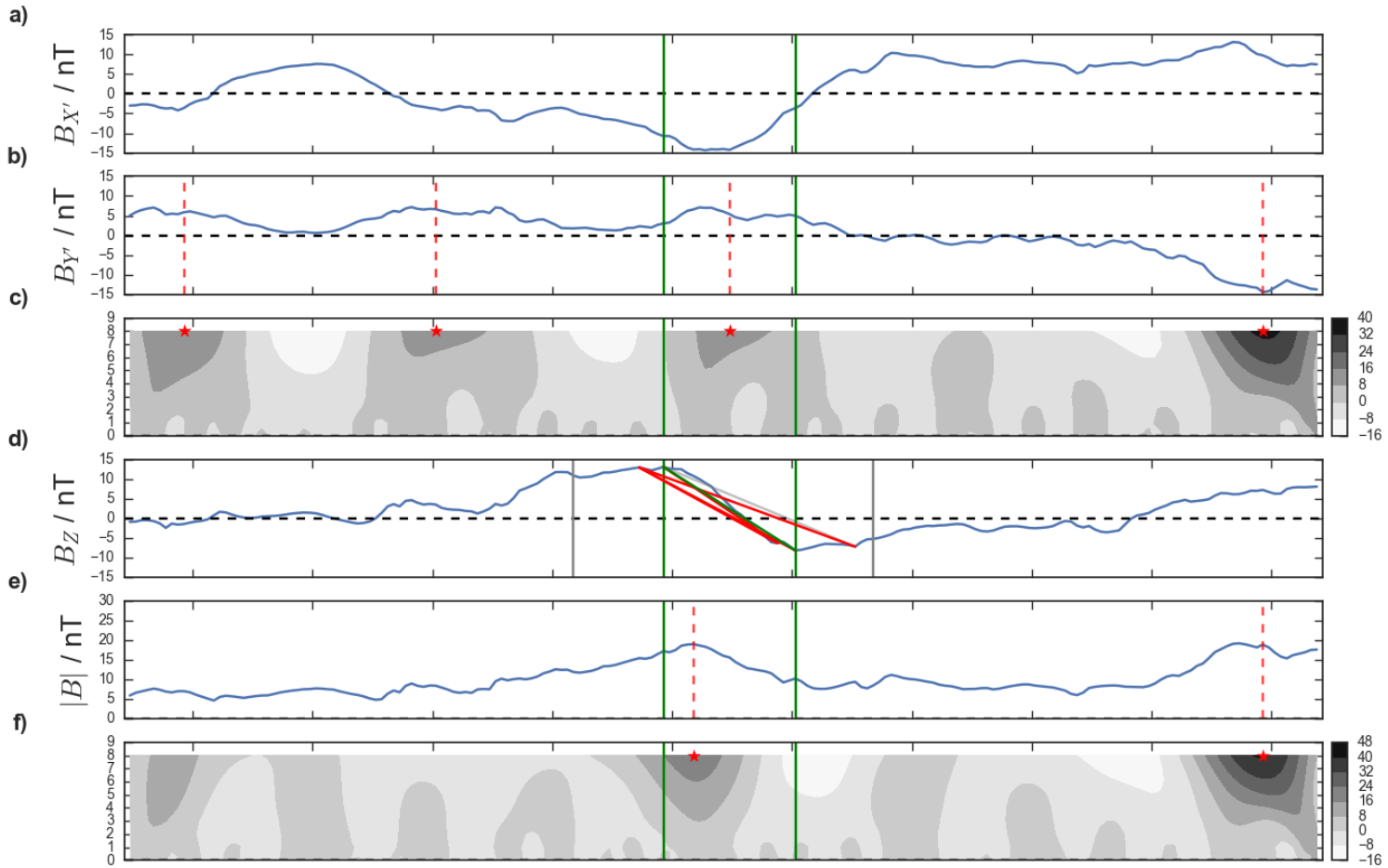
Time (UT)	09:28:00	09:28:30	09:29:00	09:29:30	09:30:00	09:30:30	09:31:00	09:31:30	09:32:00
$X'_{MSM} (R_M)$	-2.48	-2.46	-2.44	-2.42	-2.40	-2.38	-2.36	-2.34	-2.32
$Y'_{MSM} (R_M)$	0.36	0.35	0.35	0.34	0.34	0.33	0.33	0.32	0.32
$Z_{MSM} (R_M)$	-0.01	0.01	0.03	0.05	0.07	0.09	0.11	0.13	0.14



Time (UT)	09:31:17.02	09:31:17.22	09:31:17.42	09:31:17.62	09:31:17.82
$X'_{MSM} (R_M)$	-2.35	-2.35	-2.35	-2.35	-2.35
$Y'_{MSM} (R_M)$	0.32	0.32	0.32	0.32	0.32
$Z_{MSM} (R_M)$	0.12	0.12	0.12	0.12	0.12

This article is protected by copyright. All rights reserved.

pt



Time (UT)	09:31:13	09:31:14	09:31:15	09:31:16	09:31:17	09:31:18	09:31:19	09:31:20	09:31:21	09:31:22
$X'_{MSM} (R_M)$	-2.35	-2.35	-2.35	-2.35	-2.35	-2.35	-2.35	-2.34	-2.34	-2.34
$Y'_{MSM} (R_M)$	0.32	0.32	0.32	0.32	0.32	0.32	0.32	0.32	0.32	0.32
$Z'_{MSM} (R_M)$	0.11	0.12	0.12	0.12	0.12	0.12	0.12	0.12	0.12	0.12

AI

2016JA022994-f03-z-.png